

# Daily cycle of the surface layer and energy balance on the high Antarctic Plateau

DIRK VAN AS, MICHIEL VAN DEN BROEKE and RODERIK VAN DE WAL

*Institute for Marine and Atmospheric Research Utrecht (IMAU), Utrecht University, PO Box 80000, 3508 TA Utrecht, The Netherlands  
D.vanAs@phys.uu.nl*

**Abstract:** This paper focuses on the daily cycle of the surface energy balance and the atmospheric surface layer during a detailed meteorological experiment performed near Kohnen base in Dronning Maud Land, East Antarctica, in January and February 2002. Temperature, specific humidity, wind speed and the turbulent scales of these quantities, exhibit a strong daily cycle. The sensible heat flux cycle has a mean amplitude of  $\sim 8 \text{ W m}^{-2}$ , while the latent heat flux has an amplitude of less than  $2 \text{ W m}^{-2}$ , which is small compared to the amplitude of net radiation ( $\sim 35 \text{ W m}^{-2}$ ) and sub-surface heat ( $\sim 25 \text{ W m}^{-2}$ ). Between  $\sim 9$  and  $16$  h GMT convection occurs due to a slightly unstable atmospheric surface layer. At the end of the afternoon, the wind speed decreases abruptly and the mixed layer is no longer supported by the sensible heat input; the stratification becomes stable. At night a large near-surface wind shear is measured due to the presence of a nocturnal jet, which is likely to be katabatically driven, but can also be the result of an inertial oscillation. No strong daily cycle in wind direction is recorded, since both the katabatic forcing at night and the daytime forcing by the large-scale pressure gradient were directed approximately downslope during the period of measurement.

Received 16 March 2004, accepted 12 August 2004

**Key words:** atmospheric boundary layer, diurnal variability, ENABLE, snow, stability, turbulent heat flux

## Introduction

Antarctica has an important role in the global climate system; its ice sheet functions as one of the largest heat sinks in the world by extracting sensible heat from the atmosphere (Bromwich 1989). Yet relatively little is known about surface processes in the interior of the ice sheet due to its remoteness and inaccessibility. Experimental studies of the atmosphere over Antarctica and of the interaction between the ice sheet and the atmosphere can therefore greatly improve the understanding of the Antarctic climate and its role in the global atmospheric circulation.

The energy exchange between the Antarctic ice sheet and the atmosphere at a non-melting location can be described by the surface energy balance (SEB). For an infinitesimally thin surface layer without heat capacity, the SEB components are in balance:

$$SR_{in} + SR_{out} + LR_{in} + LR_{out} + H_S + H_L + G = 0, \quad (1)$$

where  $SR_{in} + SR_{out} + LR_{in} + LR_{out} = SR_{net} + LR_{net} = R_{net}$ . The first four terms in Eq. (1) denote the incoming and outgoing components of the (solar) shortwave (SR) and (terrestrial) longwave radiation (LR). Net radiation ( $R_{net}$ ) is the sum of net shortwave radiation ( $SR_{net}$ ) and net longwave radiation ( $LR_{net}$ ). The remaining non-radiative terms are the sensible heat flux ( $H_S$ ), the latent heat flux ( $H_L$ ) and the sub-surface heat flux ( $G$ ). The fluxes are defined positive when directed towards the surface.

In the long Antarctic winter, when little or no shortwave

radiation is present, the surface is cooled continuously through negative net longwave radiation. To compensate this energy loss, the turbulent and sub-surface heat fluxes extract heat from both atmosphere and ice sheet, thereby cooling the near surface air and snow. If a surface slope is present, the cold and dense layer of air adjacent to the surface is forced down-slope by a horizontal pressure gradient (katabatic wind). This situation can be maintained throughout the winter, on occasion interrupted by the horizontal advection of warm air masses or strong large-scale winds. During the summer, the absorption of shortwave radiation introduces a diurnal cycle (except for locations near the pole). The high surface albedo in the interior (0.8–0.9, Van den Broeke *et al.* 2004b) limits the amount of solar radiation available to heat the surface. However, surface warming can cause convection and the formation of a mixed layer can sometimes be observed on the plateau at daytime (Mastrantonio *et al.* 1999). Since the temperature difference between the free atmosphere and the atmospheric surface layer (ASL) is reduced, the katabatic forcing is reduced as well and the pronounced katabatic wind maximum in the lower atmospheric boundary layer (ABL) disappears. The differences between day and night are illustrated by Fig. 1, which shows mean clear sky values of potential temperature and wind speed in the lower 300 m of the atmosphere, measured by tethered balloon at Kohnen station ( $75^{\circ}00'S$ ,  $0^{\circ}04'E$ , 2892 m above sea level, Fig. 2) in January and February 2002. The night-time temperature

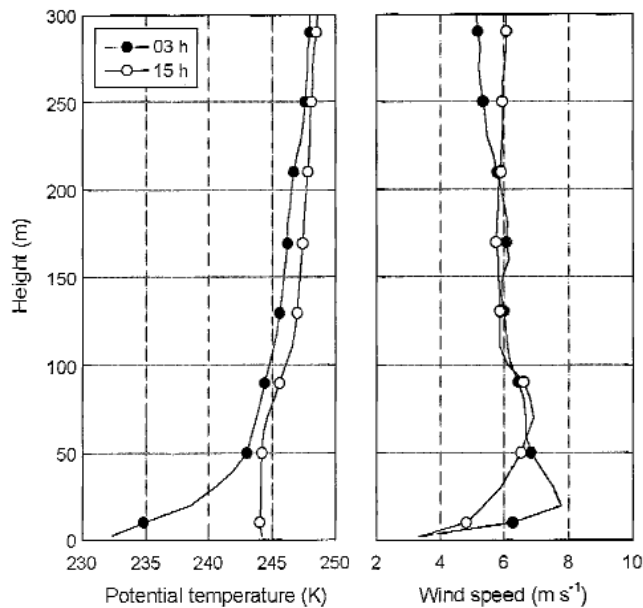


**Fig. 1.** Mean clear sky vertical profiles of potential temperature and wind speed at 3 h and 15 h GMT, measured by tethered balloon at Kohnen station in January and February 2002.

deficit in the lower 50 m of the atmosphere coincides with the presence of a nocturnal jet  $\sim 20$  m above the slightly sloping flat snow surface. From the temperature profile it is apparent that a katabatic forcing is acting in the lower 50 m of the atmosphere, but whether this is the cause of the jet remains inconclusive from the figure, as a nocturnal jet can

also be the representation of an inertial oscillation in a stably stratified layer of air.

The Antarctic SEB can be studied in several different ways. For example, general circulation models and meteorological models are useful tools to study its spatial and temporal variability (e.g. Genthon & Braun 1995, King & Connolly 1997, Van den Broeke *et al.* 1997 and Van Lipzig *et al.* 1999). Also, detailed meteorological experiments can be conducted. SEB estimates from such experiments have been presented for example by Carroll (1982), Wendler *et al.* (1988), King & Anderson (1994), Bintanja & Van den Broeke (1995), King *et al.* (1996), Bintanja (2000) and Van As *et al.* (in press). These detailed experiments can then serve to validate SEB calculations from automatic weather stations (AWSs), which provide the opportunity to calculate the year-round SEB on more remote locations. SEB estimates from AWS data have been presented, amongst others, by Stearns & Weidner (1993), Bintanja *et al.* (1997), Reijmer & Oerlemans (2002).

This paper presents the daily cycle of the SEB and ASL structure using data of a measurement campaign which was part of EPICA (European Project for Ice Coring in Antarctica). ENABLE (EPICA-Netherlands Atmospheric Boundary Layer Experiment) was performed at Kohnen station, on the east Antarctic plateau (Fig. 2) between 8 January and 9 February 2002. The diurnal variation of the SEB and/or the structure of the ASL at Antarctic locations have also been presented by e.g. Wendler *et al.* (1988), Kodama *et al.* (1989), Parish *et al.* (1993), Bintanja & Van den Broeke (1995), Van den Broeke & Bintanja (1995),

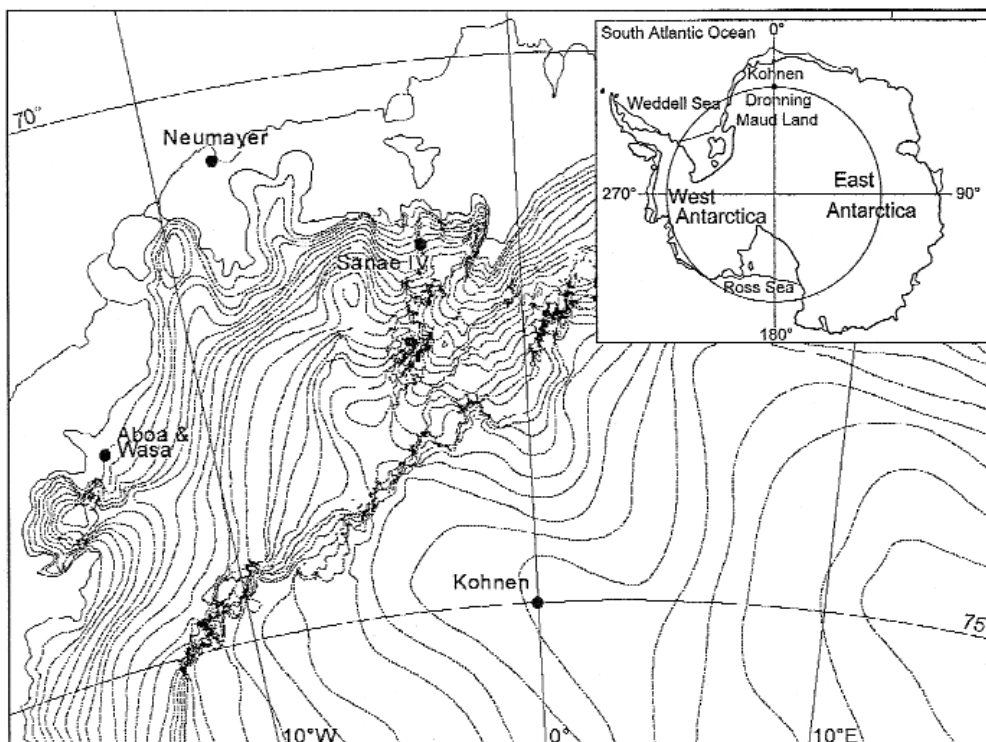


**Fig. 2.** Map of Dronning Maud Land, Antarctica. Contour lines are drawn for every 100 m of surface elevation.

Viola *et al.* (1999) and Bintanja (2000), but all of these experiments were performed at less elevated sites.

The paper is arranged as follows: firstly, the methods of calculating the SEB components will be described in the next section. Then we will discuss the general meteorological conditions at Kohlen, followed by a description of the mean clear sky daily cycle of SEB and ASL during ENABLE. Finally, a summary is presented.

### Surface energy balance calculations

The methods of measurement and SEB calculation are discussed in detail by Van As *et al.* (in press). Here a summary is given.

#### Shortwave radiation

Broadband shortwave and longwave radiation fluxes were measured in both upward and downward direction by a Kipp & Zonen CNR1 combined pyranometer and pyrriadiometer. In general, Antarctic radiation measurements can suffer from the effects of icing (SR and LR), a tilted sensor ( $SR_{in}$ ) and a poor cosine response ( $SR_{in}$ ). The deposition of ice on the sensors was generally small during ENABLE; this was checked every day. Also the horizontality of the sensor was checked daily; the tilt of the sensor did not exceed  $0.5^\circ$ . However, due to a poor cosine response of the  $SR_{in}$  sensor at zenith angles larger than  $\sim 80^\circ$ , values of albedo ( $\alpha = |SR_{out}|/SR_{in}$ ) were occasionally unrealistically high, exceeding unity, causing an underestimation of net shortwave radiation by up to  $\sim 20 \text{ W m}^{-2}$ .

This was overcome by calculating the ‘accumulated albedo’ (= running daily mean  $|SR_{out}|$  / running daily mean  $SR_{in}$ ). The results of this method are not sensitive to the poor cosine response as insolation originating from large zenith angles contributes little to the daily mean  $SR_{in}$ ; during  $\sim 30\%$  of ENABLE the solar zenith angle was larger than  $80^\circ$ , but this yielded only 7% of the total shortwave radiation flux.

Since this procedure removes the daily cycle in albedo, we added a theoretical daily cycle for a dry, clean, semi-infinite snow pack, dependent on surface snow grain size (chosen as  $10^{-4} \text{ m}$ ) and the diffuse fraction of  $SR_{in}$  (i.e. also on solar zenith angle) (Wiscombe & Warren 1980). This theoretical daily cycle of albedo contributed a maximum of 0.03 to the running mean albedo values. After this correction procedure albedo values ranged from 0.83 to 0.92 (Van As *et al.* in press). Hereafter  $SR_{net}$  was calculated from  $SR_{out}$ :

$$SR_{net} = SR_{out} (1 - \alpha). \quad (2)$$

The method is described in more detail by Van den Broeke *et al.* (2004a).

#### Turbulent heat fluxes

Turbulent heat fluxes were measured directly through eddy-correlation by Campbell CSAT3 sonic anemometers and KOH-3 Lyman- $\alpha$  hygrometers at  $\sim 2 \text{ m}$  ( $H_S$  &  $H_L$ ) and 10 m height (only  $H_S$ ). Since the sonic anemometers produced several data gaps related to power supply and low temperatures, eddy-correlation data are available for 71% of the ENABLE period. To obtain a continuous record, Van As *et al.* (in press) showed that calculated bulk fluxes can reproduce the direct measurements of the turbulent heat fluxes with good accuracy: the mean difference between calculated and measured  $H_S$  is  $-0.9 \text{ W m}^{-2}$ , the RMSD (root mean square difference) is  $3.0 \text{ W m}^{-2}$ . The mean difference for  $H_L$  is  $-0.7 \text{ W m}^{-2}$ , with a RMSD of  $1.6 \text{ W m}^{-2}$ .

According to Monin-Obukhov similarity theory the sensible and latent heat flux can be expressed as

$$H_S = \rho c_p u_* T_* \quad \text{and} \quad H_L = \rho L_s u_* q_*, \quad (3)$$

in which  $\rho$  denotes air density,  $c_p = 1005 \text{ J K}^{-1} \text{ kg}^{-1}$  is the specific heat of dry air at constant pressure and  $L_s = 2.83 \times 10^6 \text{ J kg}^{-1}$  is the latent heat of sublimation. The turbulent scales of wind speed, temperature and humidity can be approximated by the bulk method:

$$u_* = \frac{\kappa u(z)}{\ln\left(\frac{z}{z_0}\right) - \psi_m(\xi)}, \quad T_* = \frac{\kappa(T(z) - T(0))}{\ln\left(\frac{z}{z_T}\right) - \psi_T(\xi)} \quad \text{and} \quad q_* = \frac{\kappa(q(z) - q(0))}{\ln\left(\frac{z}{z_q}\right) - \psi_q(\xi)}, \quad (4)$$

where  $\kappa = 0.4$  is the Von Kármán constant,  $u$  is wind speed (measured by cup anemometers), and  $T$  and  $q$  are temperature and specific humidity, respectively, (obtained with ventilated Vaisala HMP35C probes) at height  $z$  in the surface layer.  $z_0$ ,  $z_T$  and  $z_q$  are the surface roughness lengths associated with  $u$ ,  $T$  and  $q$ . The stability correction functions for momentum ( $\psi_m$ ), heat ( $\psi_T$ ) and humidity ( $\psi_q$ ) depend solely on a non-dimensional stability parameter  $\xi = z/L_*$ . Here  $L_*$  is the Obukhov length scale, defined as

$$L_* = \frac{u_*^2 \theta_v}{g \kappa \theta_{v,*}} = \frac{u_*^2 T}{g \kappa T_*} \left( \frac{1 + 0.61q}{1 + 0.61q_*} \right) \approx \left( \frac{u_*^2 T}{g \kappa T_*} \right), \quad (5)$$

where  $g$  is the gravitational acceleration and  $\theta_v$  and  $\theta_{v,*}$  are the virtual potential temperature and its turbulent scale. The stability correction functions determined by Holtslag & De Bruin (1988) were used for stable stratifications (as recommended by Andreas 2002), and those by Paulson (1970) and Dyer (1974) for unstable stratification.

The roughness length was calculated from eddy-correlation data and was found to have a (constant) value of  $\sim 0.02 \text{ mm}$  during ENABLE (Van As *et al.* in press). We used the polynomials suggested by Andreas (1987) to calculate  $z_T$  and  $z_q$  from  $z_0$  and  $u_*$ .

Half-hourly means of  $T$  and  $u$  at height  $z = 2 \text{ m}$  serve as input for Eqs (3–5). Specific humidity is calculated from

relative humidity (RH) measurements using the equation for saturation vapour pressure of Curry & Webster (1999). Prior to this, the RH measurements were corrected according to the method proposed by Anderson (1994), as the humidity sensors measure RH with respect to water instead of ice. This introduces potentially very large errors at very low temperatures. However, because of the small  $H_L$  ( $< 1 \text{ W m}^{-2}$ ) in this temperature domain, the calculated SEB is not significantly affected.

Makkonen (1996) pointed out that these types of humidity sensors fail to record supersaturation with respect to ice, since the sensors remove supersaturation by nucleating ice crystals. Anderson (1996) however noted that supersaturation occurs infrequently at Halley, near the coast, and can be ignored. The occurrence of supersaturation on the Antarctic plateau needs further study with dewpoint sensors.

Surface temperature  $T(0)$  is determined from outgoing longwave radiation applying Boltzmann's law:

$$-LR_{out} = (1 - \varepsilon) LR_{in} + \varepsilon \sigma T(0)^4, \quad (6)$$

where  $\sigma = 5.67 \times 10^{-8} \text{ W K}^{-4} \text{ m}^{-2}$  is the Stefan-Boltzmann constant.  $\varepsilon$  is the broadband emissivity of the snow surface in the longwave part of the spectrum with a value close to unity. Due to the uncertainty of its value, here  $\varepsilon$  is set to 1. Finally, surface humidity  $q(0)$  is calculated from surface temperature assuming that the air at the snow surface is saturated with respect to ice.

#### Sub-surface heat flux

Neglecting shortwave radiation penetration in snow (justified for fine-grained Antarctic snow according to Brandt & Warren (1993)) and ventilation of the upper snow layer, the thermodynamic equation of heat transport in snow simplifies considerably. Under the assumption of horizontal homogeneity the sub-surface heat flux is then defined as:

$$G = \left( k_e \frac{\partial T}{\partial z} \right)_{z=0}, \quad (7)$$

where  $k_e$  is the effective conductivity parameter, which embodies conduction in the ice lattice, diffusive transport in air between snow grains and the sub-surface equivalents of the sensible and latent heat flux resulting from vertical gradients in temperature and specific humidity in the (saturated) air in snow. We use the empirical relationship for  $k_e$  suggested by Östin & Andersson (1991), which assumes a dependence on snow density only:

$$k_e(z) = -0.00871 + 0.439 \times 10^{-3} \rho_s(z) + 1.05 \times 10^{-6} \rho_s(z)^2. \quad (8)$$

Here  $\rho_s$  is snow density in  $\text{kg m}^{-3}$ , which was estimated from snow pit measurements during ENABLE, with values increasing from  $323 \text{ kg m}^{-3}$  to  $383 \text{ kg m}^{-3}$  between the surface and 1 m depth.

G calculations were initialised by a temperature profile

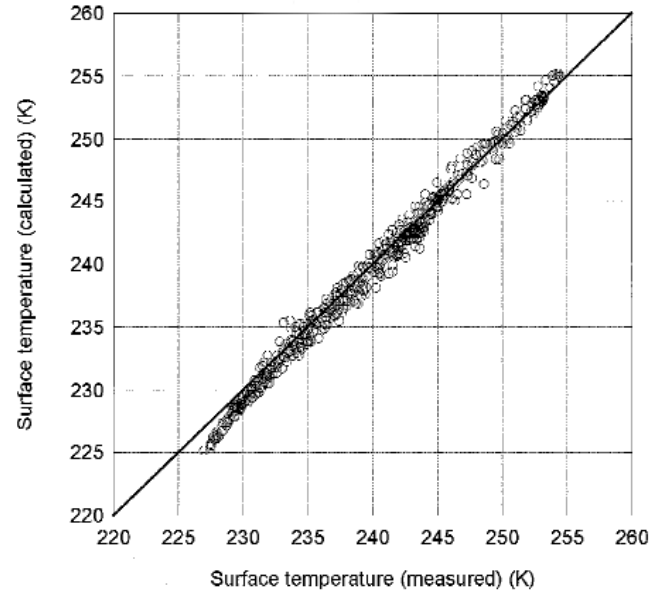


**Fig. 3.** Half-hourly calculated surface temperatures for which SEB = 0 plotted against the observed surface temperature during clear sky ENABLE days.

which was determined from thermistor string measurements at AWS 9, which is at 1.8 km distance. Temperature profiles in all subsequent time steps were calculated using  $T = T(0)$  and  $\left( \frac{\partial T}{\partial z} \right)_{z \rightarrow \infty} = 0$  as upper and lower boundary conditions, respectively. Accuracy and sensitivity of G calculations were checked by Van As *et al.* (in press). Calculated snow temperatures were found to be within 1 K of the measured snow temperatures.

#### Accuracy of the calculated SEB

To assess the accuracy of the measurements and SEB calculations we have compared the measured surface temperatures (derived from  $LR_{out}$ ) with calculated surface temperatures for days selected in this study. In the latter case we assume SEB = 0 and solve Eq. (1) for  $T(0)$ . If the two values agree, it is a testimony of accuracy for

**Table I.** Mean values of meteorological parameters at Kohnen from 1998 to 2001, during ENABLE and during the selected clear sky days of ENABLE. AWS wind speed measurements are extrapolated to 10 m height.

Parameter	Mean value (1998–2001)	Mean value (8 Jan–9 Feb 2002)	Mean value (selected clear sky days)
T (2 m)	230.0 K	245.7 K	241.1 K
q (2 m)	0.17 g kg <sup>-1</sup>	0.52 g kg <sup>-1</sup>	0.31 g kg <sup>-1</sup>
u (10 m)	4.8 m s <sup>-1</sup>	5.3 m s <sup>-1</sup>	4.8 m s <sup>-1</sup>
SR <sub>net</sub>	23 W m <sup>-2</sup>	47 W m <sup>-2</sup>	52 W m <sup>-2</sup>
LR <sub>net</sub>	-30 W m <sup>-2</sup>	-48 W m <sup>-2</sup>	-60 W m <sup>-2</sup>

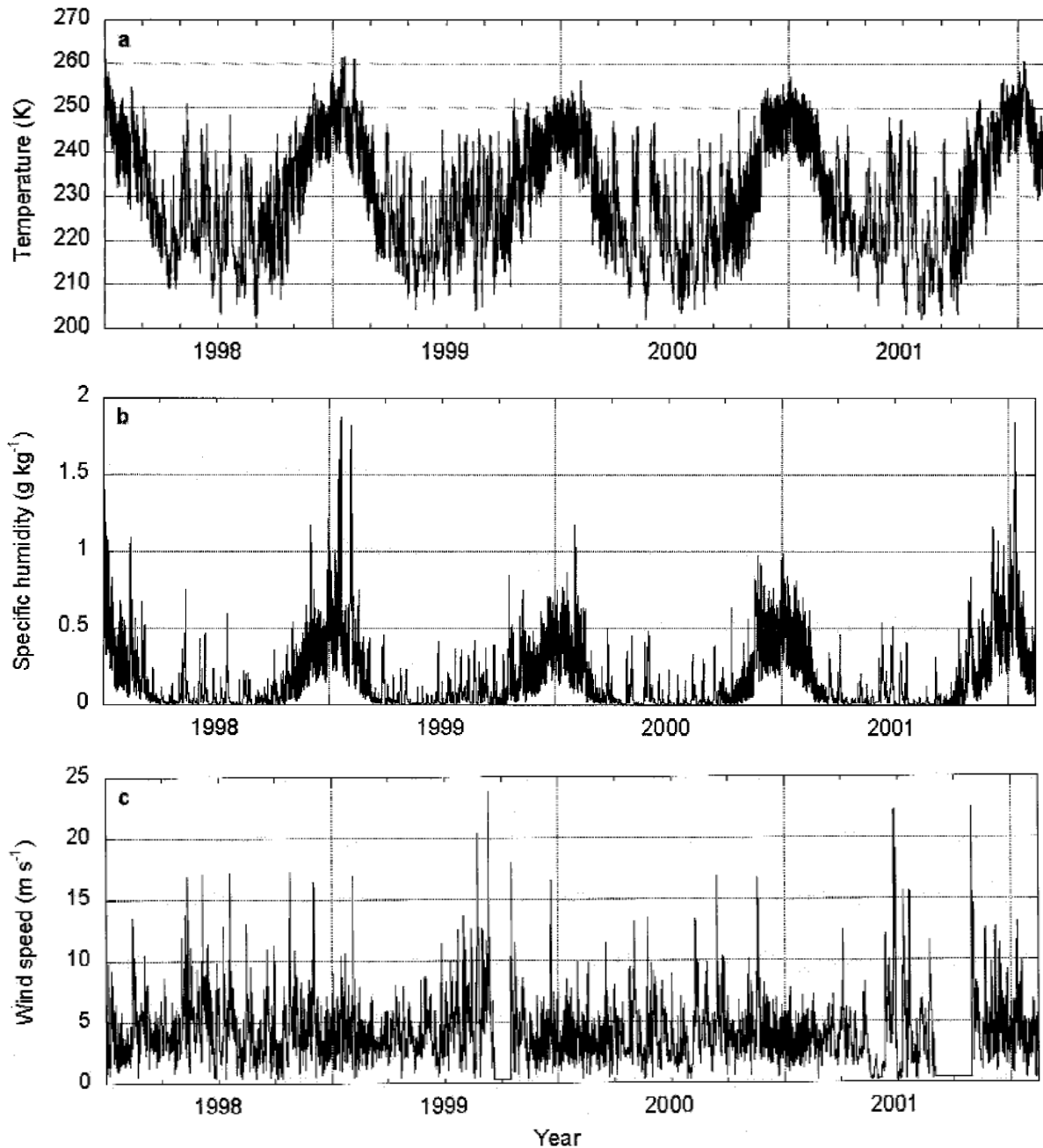


Fig. 4. Two hourly AWS data of a. 2 m temperature, b. specific humidity, and c. wind speed at Kohnen over the four year period prior to and including ENABLE. Gaps in wind speed data occur when the sensor is fixed by icing.

(radiation) measurements and calculated components ( $H_S$ ,  $H_L$  and  $G$ ).

Figure 3 shows that there is good agreement between the 30 minute mean calculated and measured surface temperatures. The RMSD between calculations and measurements is only 0.9 K, which is equivalent to a surface flux of approximately  $2.7 \text{ W m}^{-2}$ . We feel that this is a good result for a SEB study under difficult conditions, and suffices especially when the focus is not on absolute values.

Furthermore, in several figures in this paper the standard

deviation is indicated. As will become clear, the typical day to day variability in most measured parameters is much more significant than their random measurement error, but does still not dominate the daily cycle.

## Results

### *General meteorological conditions*

Kohnen station is situated on the eastern Antarctic plateau, approximately 550 km from the South Atlantic coastline.

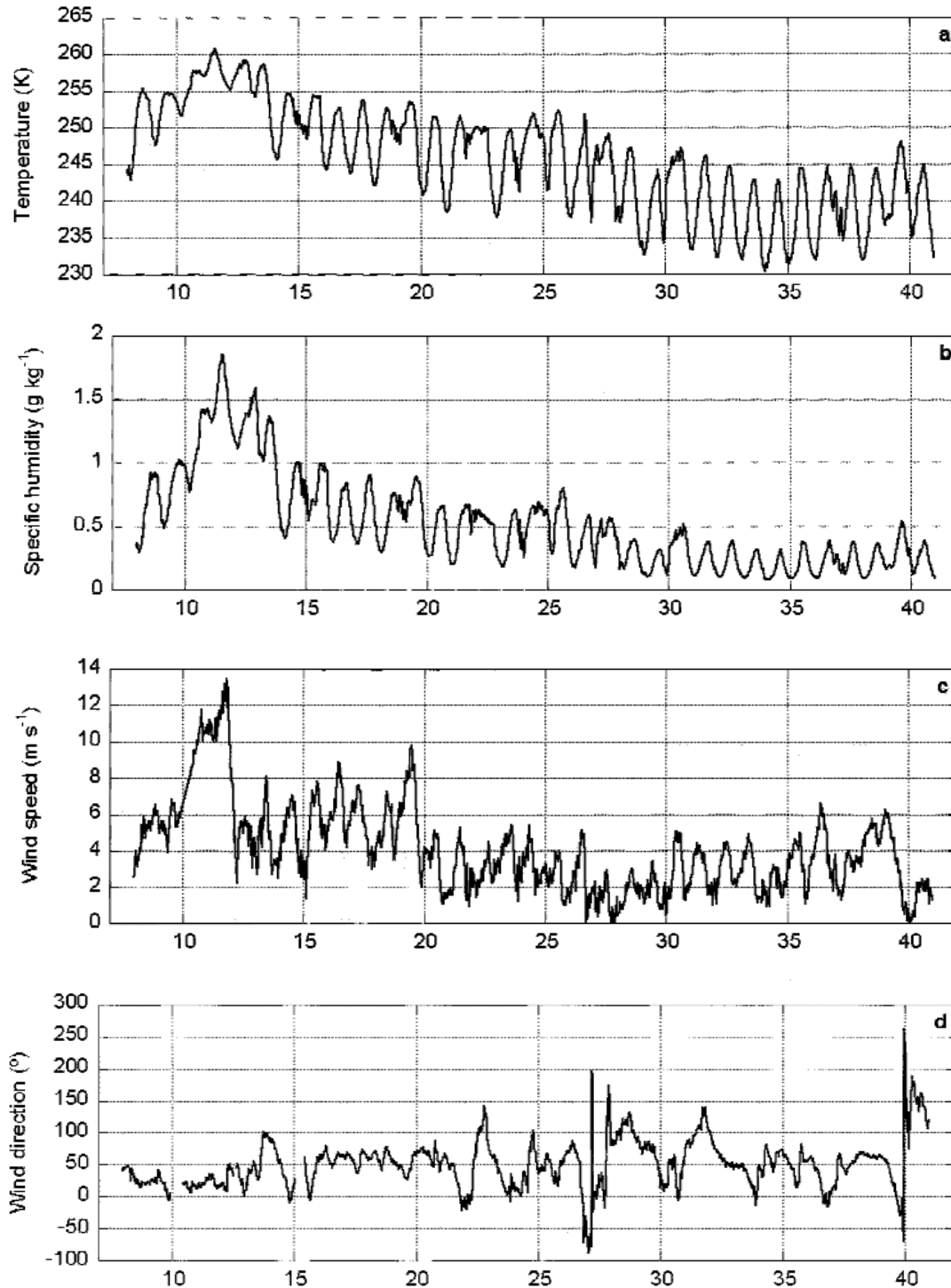


Fig. 5. Half-hourly means of a. 2 m temperature, b. specific humidity, c. wind speed, and d. wind direction during ENABLE.

AWS 9 has been in operation at this location since the austral summer of 1997/98. Figure 4 presents two hour means of AWS data of the four year period prior to and including ENABLE and Fig. 5 shows half-hourly means of T, q, u and wind direction (wd) during ENABLE. Basic climatological means and ENABLE means are given in Table I. The climate at Kohnen is dry and cold, with weak

winds compared to Antarctic coastal sites or the escarpment region. During the experiment, mean 2 m temperature, specific humidity and 10 m wind speed were  $\sim 245.7$  K,  $0.52 \text{ g kg}^{-1}$  and  $5.3 \text{ m s}^{-1}$ , respectively, which is within the recorded variability of the same period in the four previous years as determined from the AWS data. Net shortwave radiation was slightly low during ENABLE ( $\sim 47 \text{ W m}^{-2}$ )

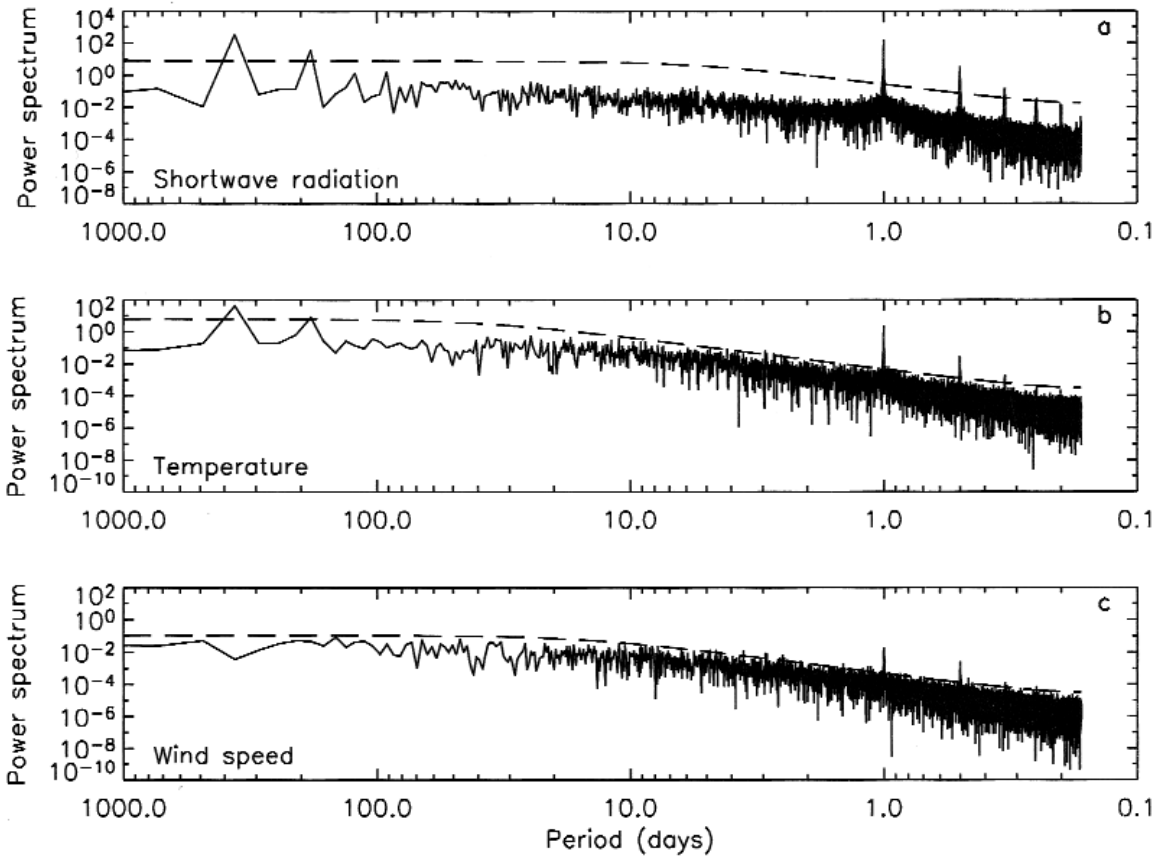


Fig. 6. Power spectra of **a.** net shortwave radiation, **b.** 2 m temperature, and **c.** 2 m wind speed, measured by AWS 9 over a four year period. The dashed lines are the 99% significance level.

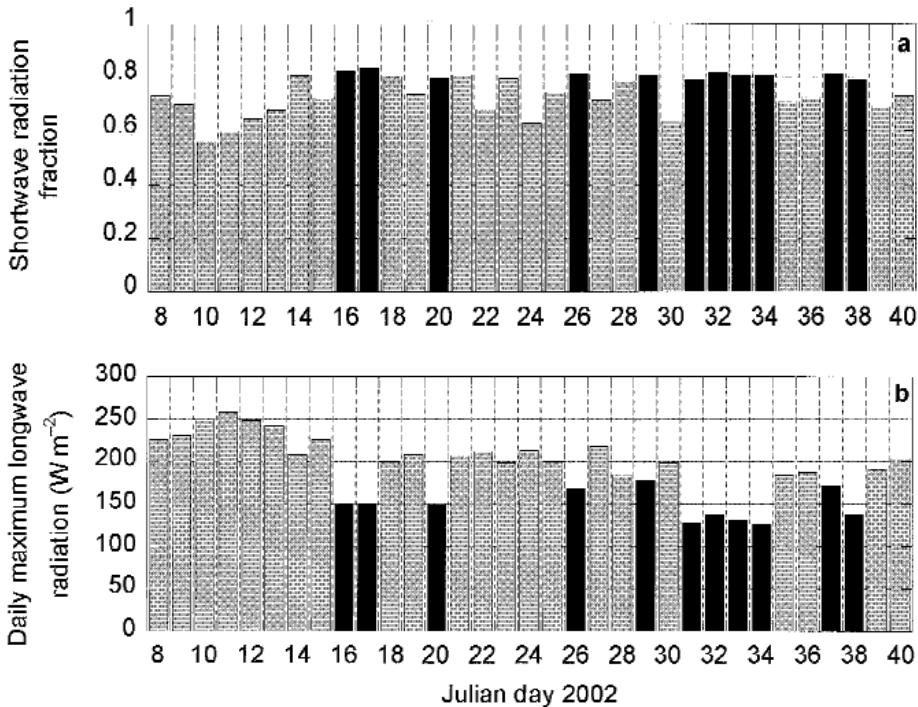
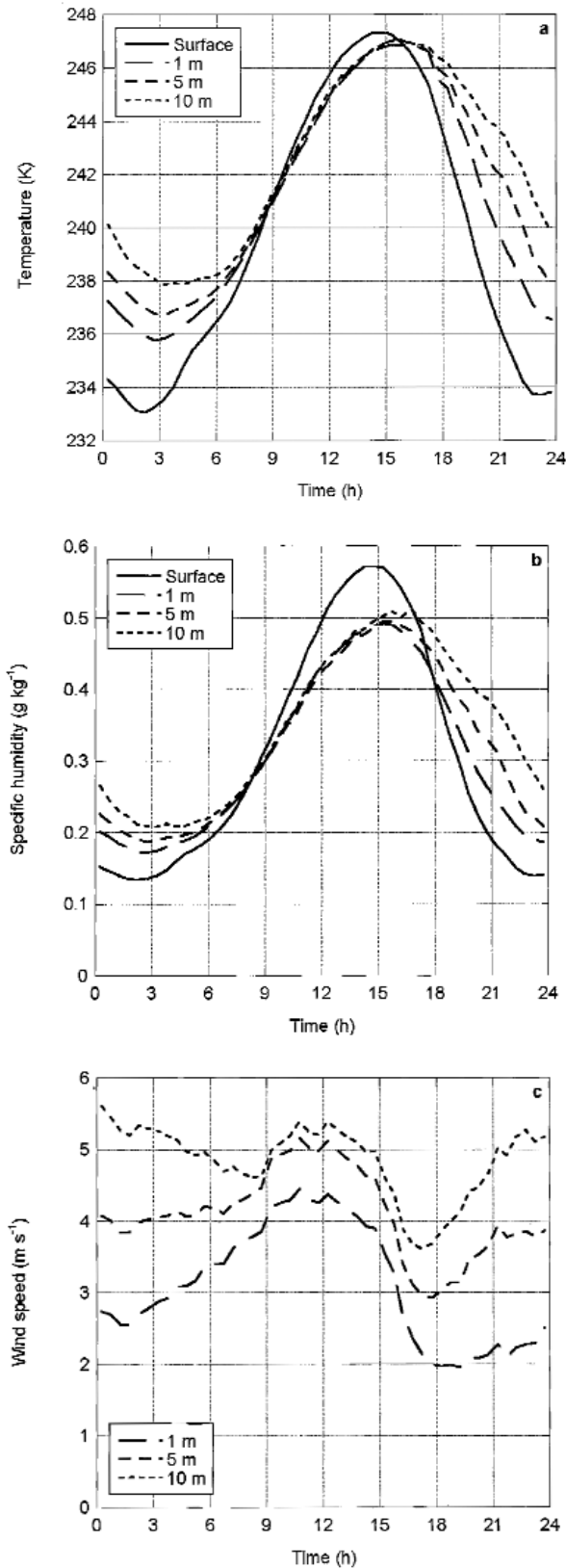


Fig. 7. **a.** The ratio of daily means of  $SR_{in}$  at the surface and at the top of the atmosphere, and **b.** the daily maximum of  $LR_{in}$  during ENABLE. Black bars denote the clear sky days used in this study, grey bars denote the remaining days.



**Fig. 8.** The mean daily cycles of **a.** temperature, **b.** specific humidity, and **c.** wind speed at 10, 5 and 1 m height and at the surface over eleven clear sky days during ENABLE.

and net longwave radiation somewhat high ( $\sim -48 \text{ W m}^{-2}$ ), which is at least partially caused by the passage of a low pressure system at the beginning of the campaign (Fig. 5).

To illustrate on which timescales the near-surface variability at Kohnen dominates, the power spectra of 2 h mean  $\text{SR}_{\text{net}}$ ,  $T$  and  $u$  at  $\sim 2 \text{ m}$  height from the four year AWS dataset are shown in Fig. 6. In spite of the short summer period the figure shows a strong daily cycle for all three parameters, well exceeding the 99% significance level which is indicated by dashed lines. The pronounced daily cycle is clearly visible in Fig. 5 as well. Figure 6 also shows a significant yearly cycle in  $\text{SR}_{\text{net}}$  and  $T$ , but not in the wind speed data. The higher harmonics of the daily and yearly cycles are a result of the limitations of the Fast Fourier Transform as they are caused by the non-sinus shaped cycles of the daily and annual signals. A dominant variability on synoptic timescales is not clearly identifiable. The 99% significance level is slightly exceeded by spectral peaks in temperature and wind speed at an oscillation period of approximately three days.

The direction and the high directional constancy (0.88, Reijmer 2001) of the near-surface winds at Kohnen suggest that katabatic winds occur frequently here, in spite of the small surface slope of  $1.3 \pm 0.3 \text{ m km}^{-1}$  in east/northeasterly direction ( $\sim 61^\circ$ ) (derived from the Radarsat Antarctic Mapping Project digital elevation model version 2 (Liu *et al.* 2001)). Figure 5d shows that near-surface wind had the tendency to blow in the approximate down-slope direction during ENABLE, with a mean direction of  $49^\circ$ . During the strong-wind event at the beginning of ENABLE the wind turned towards a more northerly direction.

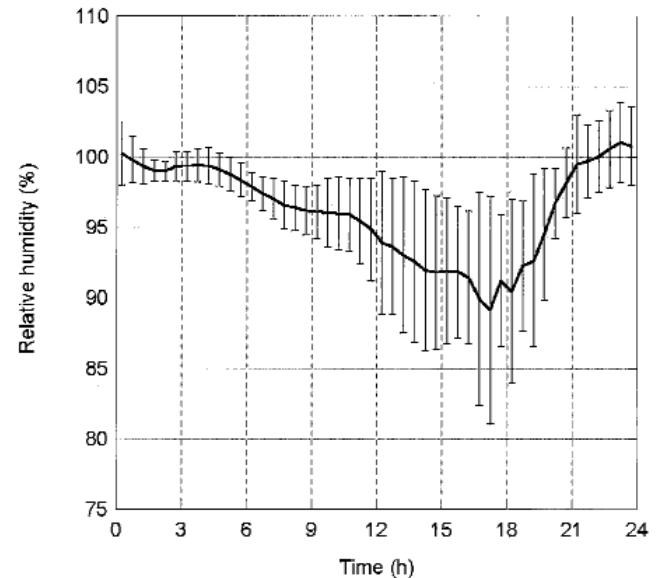


**Fig. 9.** The mean clear sky daily cycle of relative humidity (with respect to ice) at 2 m height during ENABLE. The bars indicate the standard deviation.

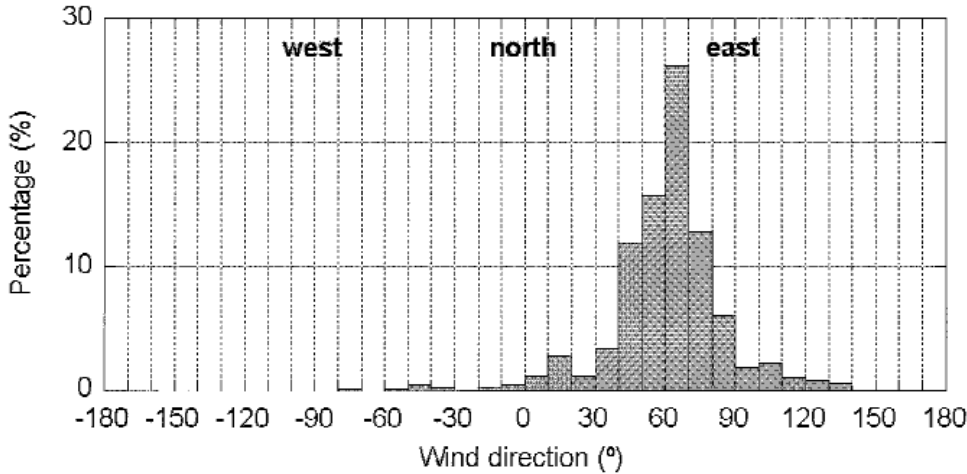


**Fig. 10.** Wind direction distribution at 2 m height during the eleven clear sky days of ENABLE. The surface-slope direction is  $\sim 61^\circ$ .

### Mean clear sky daily cycle

#### Data selection

From ENABLE data, we selected days with a pronounced daily cycle. Since shortwave radiation forces the daily cycle, these days are characterized by clear skies. Fig. 7a shows the ratio of daily mean incoming shortwave radiation at the surface to its value at the top of the atmosphere for all ENABLE days. Partial cloud cover or overcast conditions during daytime result in lower ratios and are excluded from this study. A second method to identify cloudiness during a day is through  $LR_{in}$ , as high values of  $LR_{in}$  signify a high liquid water content of the atmosphere. The daily maximum values of  $LR_{in}$  are plotted in Fig. 7b. This enables us to eliminate days with night-time cloudiness, since these are not recognized in Fig. 7a. From here on, the results presented in this paper will describe the average daily cycle of the eleven clear sky days during ENABLE, indicated by black bars in Fig. 7. Icing occurred on multiple sensors on 28 January due to the presence of a fog layer; therefore this day is excluded as well. Table I shows that the mean temperature, specific humidity and wind speed of the selected days are lower than their mean ENABLE values. Although  $SR_{net}$  is higher in clear sky conditions, the surface is cooled more strongly through a more negative net radiation.

#### Temperature, humidity, wind speed and wind direction

Figure 8 shows the mean clear sky daily cycle in temperature, specific humidity and wind speed at the approximate heights of 10, 5 and 1 m and at the surface. During the first part of the day,  $T$  and  $q$  strongly increase with height and a large wind shear is present. From  $\sim 2$  h GMT onwards, the surface starts to warm. The air temperatures at the three presented heights start to increase  $\sim 0.5$  to 2 h later. Specific humidity shows similar behaviour because of the strong dependence of saturation vapour pressure on temperature and the near saturation of the air. Wind shear decreases significantly during these morning hours, as stability decreases.

At approximately 9 h GMT convection starts as surface temperature exceeds the temperatures in the ASL. Mean surface specific humidity exceeds the atmospheric humidity values slightly earlier, indicating the start of sublimation at  $\sim 8$  h. From this moment, wind speed in the ASL increases uniformly until it reaches a maximum around noon. The maximum surface temperature and specific humidity occur at  $\sim 15$  h, again peaking  $\sim 1$  h before the air temperatures and specific humidity values do. Striking is the large variation of surface temperatures in excess of 14 K during the daily cycle. After approximately 16 h, temperature and specific humidity decrease. During this collapse of the convective system, the wind speed drops rapidly. A clear minimum is recorded between 17 h and 18 h at all heights. In the evening, a large wind shear is again recorded.

The daily cycle of relative humidity (with respect to ice) at 2 m height is plotted in Fig. 9. Only one level is shown,

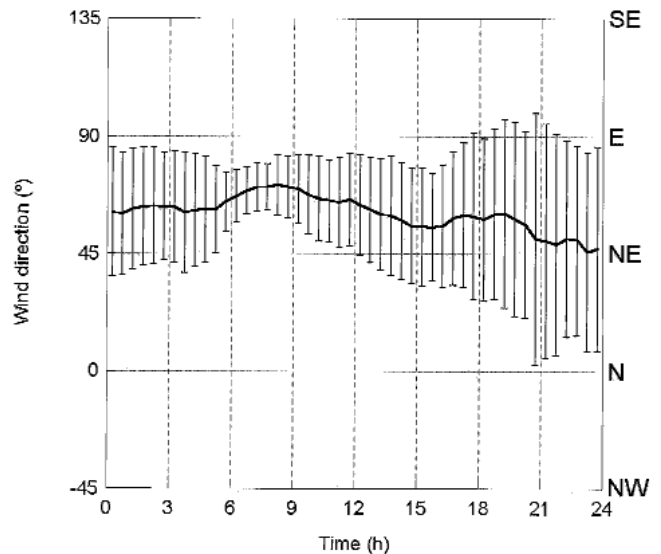


**Fig. 11.** The mean clear sky daily cycle of wind direction at 2 m height during ENABLE. The bars indicate the standard deviation.

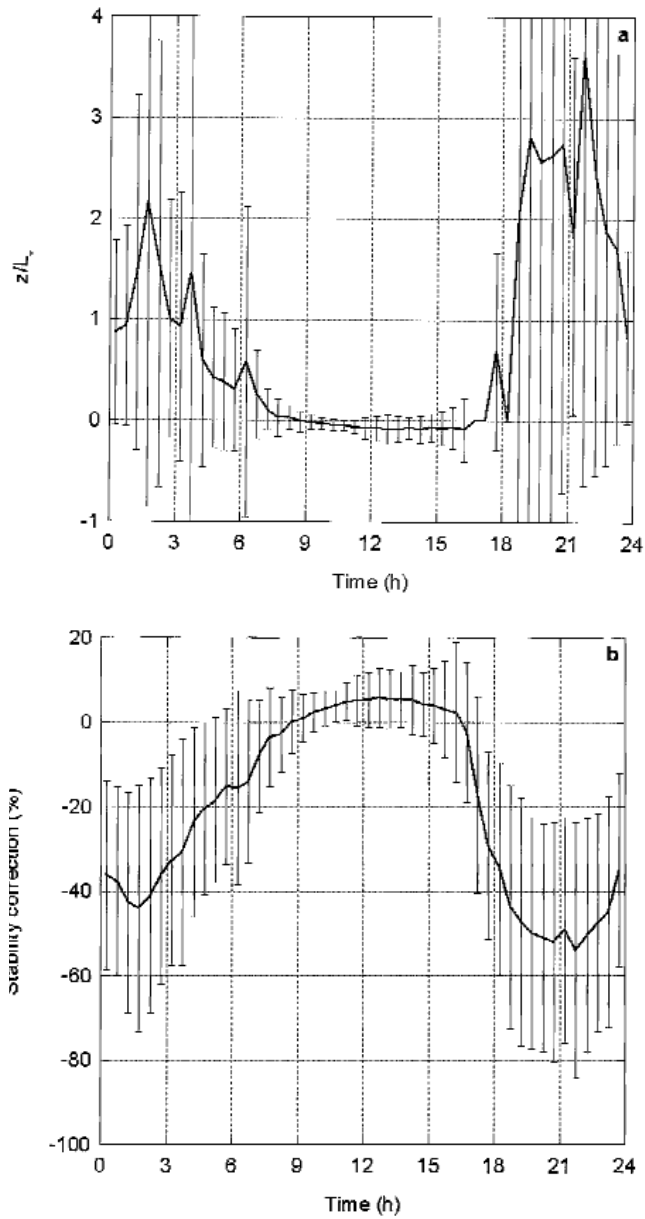


**Fig. 12.** The mean clear sky daily cycle of **a.** stability parameter  $z/L_*$  and **b.** its effect on the magnitude of the turbulent heat fluxes (see Eq. 4) during ENABLE. The bars indicate the standard deviation.

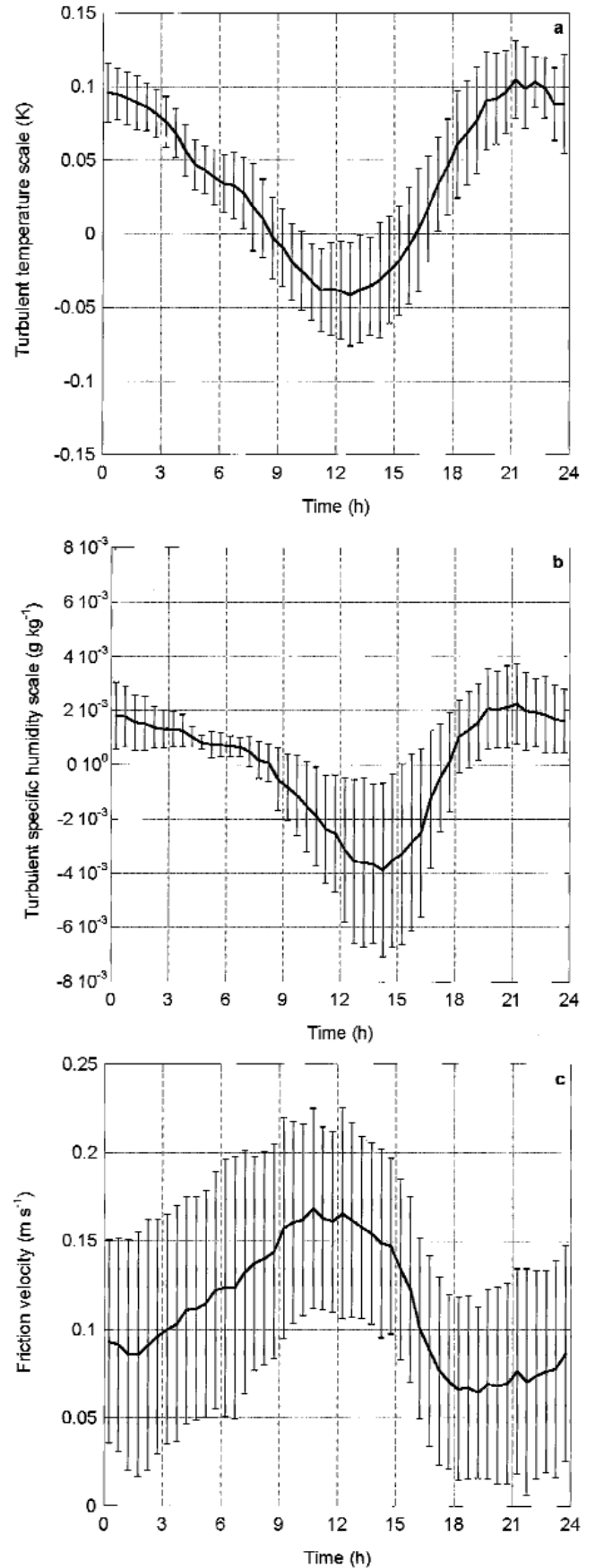


**Fig. 13.** (opposite column) The mean daily cycles of the turbulent scales of **a.** temperature, **b.** specific humidity, and **c.** wind speed over eleven clear sky days during ENABLE. The bars indicate the standard deviation.

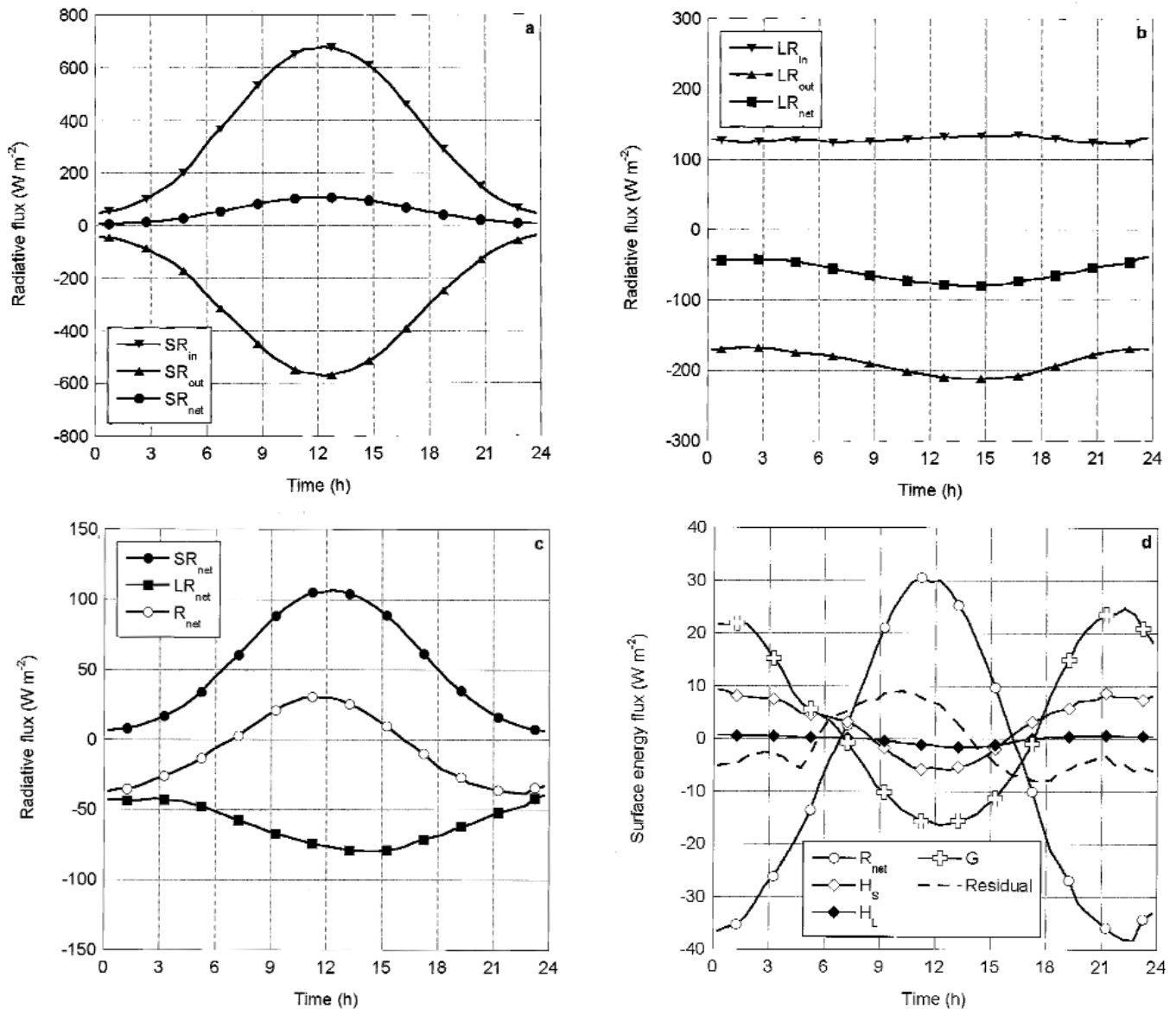


**Fig. 14.** The mean daily cycles of **a.** SR, **b.** LR, **c.**  $R_{net}$ , and of **d.**  $R_{net}$ ,  $H_s$ ,  $H_L$ ,  $G$  and the energy residual over eleven clear sky days during ENABLE.

because there is not much variation with height. At the end of the evening and beginning of the night the air is saturated. RH decreases from  $\sim 4$  h GMT onwards, which is caused by rising temperatures, until a minimum value of  $\sim 89\%$  is reached at the end of the afternoon. From then on RH increases again. The figure does not show a large daily cycle; the air of the ASL is near saturation the entire day. We note that values indicating supersaturation in Fig. 9 are spurious readings as the instruments are not capable of measuring  $RH > 100\%$ . Supersaturation is likely to occur and needs attention in future experiments.

Wind directional constancy at 2 m during the eleven clear sky days of ENABLE is very high with a value of 0.95. Figure 10 shows that the wind blows persistently from an east/north-easterly direction during these days. This

direction is close to the slope direction of  $\sim 61^\circ$ . Figure 11 shows the mean clear sky daily cycle of wind direction during ENABLE. The down-slope wind direction at night is consistent with the behaviour of a katabatic wind, but a rotation to the left due to the Coriolis force is not observed. During the day the wind direction in the mixed layer is most likely determined by large scale winds and is also east/north-easterly. We can identify a slight anti-clockwise rotation of the wind vector between  $\sim 9$  h and 16 h GMT. The standard deviation shows that the daytime variability in wind direction is smaller than at night.

#### Stability and turbulent scales

Figure 12a shows the mean clear sky daily cycle of the stability parameter  $\chi = z/L_*$ , which is positive for stable

stratification and negative for an unstably stratified layer. The figure indicates slightly unstable conditions between approximately 9 h and 17 h GMT. The remainder of the day the stratification is stable. Stability peaks between 19 h and 22 h, after an increase early in the evening. This happens rapidly in comparison with the relatively gradual decrease in stability in the first part of the day. Standard deviation is large but can be understood from the non-linear dependence of  $z/L_*$  on  $u_*$  and the large day to day variability in  $u_*$  as will be shown below. However, the daily cycle in stability is similar for all eleven clear sky days.

The behaviour of  $z/L_*$  can be understood from the diurnal variability in the turbulent scales  $u_*$  and  $T_*$  (Eq. 5 shows that  $z/L_*$  is fairly independent of  $q_*$ ). The sign of stability parameter  $z/L_*$  is fully determined by  $T_*$ . A high friction velocity  $u_*$  acts to increase the absolute value of  $L_*$  through enhanced vertical mixing. From this, we expect maximum stability to occur when  $u_*$  is small and  $T_*$  is large and positive. This is confirmed by Fig. 13, in which  $T_*$ ,  $q_*$  and  $u_*$  are plotted. The sudden increase in stability in the early evening is caused by low near-surface wind speeds. The noontime maximum in  $u_*$  coincides with negative values of  $T_*$  which results in slightly unstable conditions. Friction velocity peaks  $\sim 2$  and  $3$  h before  $T_*$  and  $q_*$  do, respectively. Furthermore,  $T_*$  and  $q_*$  obtain their minimum values when gradients in  $T$  and  $q$  are largest, which occurs prior to the maximum in air temperature and specific humidity (Fig. 8). Standard deviation is relatively large for  $u_*$  due to the day to day differences in daily mean wind speed. However, the shape of the daily cycle of  $u_*$  is similar for all eleven clear sky days.

To investigate how the stability parameter influences the turbulent heat fluxes through Eq. (4), we have plotted the contribution of the stability correction parameter  $\gamma$  to the absolute value of the turbulent heat fluxes in Fig. 12b. Clearly the influence is large. During daytime the correction increases the fluxes only by  $\sim 6\%$ , but at night the stability correction reduces the turbulent heat fluxes by  $\sim 50\%$ .

#### Surface energy balance

Figure 14a shows that the mean incoming solar radiation over the eleven clear sky days during ENABLE contributes a maximum of approximately  $680 \text{ W m}^{-2}$  at noon to the surface energy balance. Most of this is reflected at the surface due to the high surface albedo (mean value of  $\sim 0.86$  during ENABLE), leaving a maximum of  $107 \text{ W m}^{-2}$  for net shortwave radiation. Incoming and outgoing longwave radiation are relatively small due to the low temperatures in the atmosphere and at the surface.  $LR_{\text{out}}$  displays a strong daily cycle due to the daily temperature variation of the surface (Fig. 14b).  $LR_{\text{in}}$  has an amplitude of  $\sim 6 \text{ W m}^{-2}$  over a day; the maximum value is attained in the afternoon, when the ABL temperature peaks. The surface loses energy through  $LR_{\text{net}}$ . Since the surface continues to warm even after the maximum in  $SR_{\text{net}}$  (Fig. 8a),  $LR_{\text{net}}$  lags  $SR_{\text{net}}$  by

approximately three hours. Figure 14c shows that this phase difference results in a maximum in net radiation approximately one hour before noon with a value of  $\sim 30 \text{ W m}^{-2}$ .

In spite of its small value,  $R_{\text{net}}$  dominates the SEB, as shown in Fig. 14d. The other components, of which the  $G$  has the greatest magnitude, all tend to counteract  $R_{\text{net}}$ . From Fig. 13 we expect a negative  $H_s$  between approximately 9 h and 16 h GMT and a negative  $H_L$  between 8 h and 18 h GMT, which is confirmed by Fig. 14d. Due to the small values of the surface roughness lengths and the limited amount of solar radiation,  $H_s$  and  $H_L$  are small, contributing less than  $9 \text{ W m}^{-2}$  and  $2 \text{ W m}^{-2}$  to the mean SEB, respectively. The latent heat flux is especially small due to the small gradients in specific humidity, owing to the low temperatures.

The SEB components have all been determined independently. According to Eq. (1) the components should be balanced for a non-melting skin surface layer without heat capacity. The residual energy plotted in Fig. 14d is the sum of all components and shows that this condition has not been met entirely. This residual energy can be attributed to sensor and calculation inaccuracies.

#### Summary

In this paper we presented the summertime clear sky daily cycle of near-surface meteorological variables and the surface energy balance near Kohonen base, located on the high Antarctic plateau. Absorbed solar radiation drives the diurnal cycle in the other components of the SEB, even though the high albedo ( $\sim 0.86$ ) results in only a relatively small  $SR_{\text{net}}$ . Since  $LR_{\text{net}}$  reaches a minimum value at  $\sim 14\text{--}15$  h GMT, when surface temperature is high,  $R_{\text{net}}$  peaks just before noon. The turbulent heat fluxes and the sub-surface heat flux distribute the surplus radiative energy over the ASL and the upper snow layer. In spite of large near-surface temperature gradients, the mean turbulent heat fluxes are small due to the low surface roughness and generally weak winds. Between  $\sim 9$  and  $16$  h surface temperatures exceed air temperatures, which results in weak convection. A short-lived, shallow mixed layer is formed in the otherwise stably stratified ASL.  $T_*$  and  $q_*$  reach their maximum values before  $T(0)$  and  $q(0)$  do around  $14\text{--}15$  h, while  $u_*$  and  $u$  peak simultaneously around noon. The directional constancy at daytime is remarkably high, which is proof of a stationary large-scale setting. After  $\sim 16$  h stability rapidly increases due to an increase in  $T_*$  and a sudden drop in  $u_*$ . Maximum stability is reached between  $\sim 19$  h and  $22$  h, when  $T_*$  and  $u_*$  attain their maximum and minimum values, respectively. In this stable layer a nocturnal jet develops. Although the jet is located in the layer of temperature deficit and it is directed in the down-slope direction, further analysis is necessary to determine whether this jet is entirely katabatically driven, or partially

is a manifestation of an inertial oscillation.

### Acknowledgements

We thank our German colleagues from the Alfred Wegener Institute (AWI) for hosting the experiment and Wim Boot and Henk Snellen for technical support. Furthermore, we thank Michiel Helsen and the other members of the 'Ice and Climate' group of the Institute for Marine and Atmospheric research in Utrecht (IMAU). This work is partly funded by the Netherlands Polar Programme (NPP) and is a contribution to the 'European Project for Ice Coring in Antarctica' (EPICA), a joint ESF (European Science Foundation)/EC scientific programme, funded by the European Commission and by national contributions from Belgium, Denmark, France, Germany, Italy, the Netherlands, Norway, Sweden, Switzerland and the United Kingdom. This is EPICA publication number 115.

### References

- ANDERSON, P.S. 1994. A method for rescaling humidity sensors at temperatures well below freezing. *Journal of Atmospheric and Ocean Technology*, **11**, 1388–1391.
- ANDERSON, P.S. 1996. Reply to "Comments on 'A method for rescaling humidity sensors at temperatures well below freezing'". *Journal of Atmospheric and Ocean Technology*, **13**, 913–914.
- ANDREAS, E.L. 1987. A theory for the scalar roughness and the scalar transfer coefficients over snow and sea ice. *Boundary-Layer Meteorology*, **38**, 159–184.
- ANDREAS, E.L. 2002. Parameterizing scalar transfer over snow and ice: a review. *Journal of Hydrometeorology*, **3**, 417–432.
- BINTANJA, R. 2000. Surface heat budget of Antarctic snow and blue ice: interpretation of spatial and temporal variability. *Journal of Geophysical Research*, **105**, 24387–24407.
- BINTANJA, R. & VAN DEN BROEKE, M.R. 1995. The surface energy balance of Antarctic snow and blue ice. *Journal of Applied Meteorology*, **34**, 902–926.
- BINTANJA, R., JONSSON, S. & KNAP, W.H. 1997. The annual cycle of the surface energy balance of Antarctic blue ice. *Journal of Geophysical Research*, **102**, 1867–1881.
- BRANDT, R.E. & WARREN, S.G. 1993. Solar-heating rates and temperature profiles in Antarctic snow and ice. *Journal of Glaciology*, **39**, 99–110.
- BROMWICH, D. H. 1989. Satellite analyses of Antarctic katabatic wind behavior. *Bulletin of the American meteorological society*, **70**, 738–749.
- CARROLL, J.J. 1982. Long-term means and short-term variability of the surface energy balance components at the South Pole. *Journal of Geophysical Research*, **87**, 4277–4286.
- CURRY, J.A. & WEBSTER, P.J. 1999. *Thermodynamics of atmospheres and oceans*. London: Academic Press, 467 pp.
- DYER, A.J. 1974. A review of flux-profile relationships. *Boundary-Layer Meteorology*, **7**, 363–372.
- GENTHON, C. & BRAUN, A. 1995. ECMWF analyses and predictions of the surface climate of Greenland and Antarctica. *Journal of Climate*, **8**, 2324–2332.
- HOLTSLAG, A.A.M. & DE BRUIN, H.A.R. 1988. Applied modelling of the night-time surface energy balance over land. *Journal of Applied Meteorology*, **27**, 689–704.
- KING, J.C. & ANDERSON, P.S. 1994. Heat and water-vapor fluxes and scalar roughness lengths over an Antarctic ice shelf. *Boundary-Layer Meteorology*, **69**, 101–121.
- KING, J.C. & CONNOLLEY, W.M. 1997. Validation of the surface energy balance over the Antarctic ice sheets in the UK. Meteorological Office Unified Climate Model. *Journal of Climate*, **10**, 1273–1287.
- KING, J.C., ANDERSON, P.S., SMITH, M.C. & MOBBS, S.D. 1996. The surface energy and mass balance at Halley, Antarctica during winter. *Journal of Geophysical Research*, **101**, 19119–19128.
- KODAMA, Y., WENDLER, G. & ISHIKAWA, N. 1989. The diurnal variation of the boundary layer in summer in Adelie Land, Eastern Antarctica. *Journal of Applied Meteorology*, **28**, 16–24.
- LIU, H., JEZEK, K., LI, B. & ZHAO, Z. 2001. *Radarsat Antarctic Mapping Project digital elevation model version 2*. Boulder, CO: National Snow and Ice Data Center, digital media.
- MAKKONEN, L. 1996. Comments on "A method for rescaling humidity sensors at temperatures well below freezing". *Journal of Atmospheric and Ocean Technology*, **13**, 911–912.
- MASTRANTONIO, G., MALVESTUTO, V., ARGENTINI, S., GEORGIADIS, T. & VIOLA, A. 1999. Evidence of a convective boundary layer developing on the Antarctic Plateau during the summer. *Meteorology and Atmospheric Physics*, **71**, 127–132.
- ÖSTIN, R. & ANDERSSON, S. 1991. Frost growth parameters in a forced air stream. *International Journal of Heat Mass Transfer*, **34**, 1009–1017.
- PARISH, T.R., PETTRE, P. & WENDLER, G. 1993. A numerical study of the diurnal-variation of the Adélie Land katabatic wind regime. *Journal of Geophysical Research*, **98**, 12933–12947.
- PAULSON, C.A. 1970. The mathematical representation of wind speed and temperature profiles in the unstable atmospheric surface layer. *Journal of Applied Meteorology*, **9**, 857–861.
- REIJMER, C.H. 2001. *Antarctic meteorology: a study with automatic weather stations*, PhD thesis, Utrecht University, 158 pp. [Unpublished]
- REIJMER, C.H. & OERLEMANS, J. 2002. Temporal and spatial variability of the surface energy balance in Dronning Maud Land, East Antarctica. *Journal of Geophysical Research*, **107**, 4759.
- STEARNS, C.R. & WEIDNER, G.A. 1993. Sensible and latent heat flux estimates in Antarctica. *Antarctic Research Series*, **61**, 109–138.
- VAN AS, D., VAN DEN BROEKE, M.R., REIJMER, C.H. & VAN DE WAL, R.S.W. In press. The summer surface energy balance of the high Antarctic plateau. *Boundary-Layer Meteorology*.
- VAN DEN BROEKE, M.R. & BINTANJA, R. 1995. Summertime atmospheric circulation in the vicinity of a blue ice area in Queen Maud Land, Antarctica. *Boundary-Layer Meteorology*, **72**, 411–438.
- VAN DEN BROEKE, M.R., VAN DE WAL, R.S.W. & WILD, M. 1997. Representation of Antarctic katabatic winds in a high resolution GCM and a note on their climate sensitivity. *Journal of Climate*, **10**, 3111–3130.
- VAN DEN BROEKE, M.R., VAN AS, D., REIJMER, C.H. & VAN DE WAL, R.S.W. 2004a. Assessing and improving the quality of unattended radiation observations in Antarctica. *Journal of Atmospheric and Ocean Technology*, **21**, 1417–1431.
- VAN DEN BROEKE, M.R., REIJMER, C.H. & VAN DE WAL, R.S.W. 2004b. Surface radiation balance in Antarctica as measured with automatic weather stations. *Journal of Geophysical Research*, **109** (D9), D09103, 10.1029/2003JD004394.
- VAN LIPZIG, N.P.M., VAN MEIJGAARD, E. & OERLEMANS, J. 1999. Evaluation of a regional atmospheric model using measurements of surface heat exchange processes from a site in Antarctica. *Monthly Weather Review*, **127**, 1994–2011.
- VIOLA, A.P., PETENKO, I., MASTRANTONIO, G. ARGENTINI, S. & BEZVERHNII, V. 1999. Diurnal variations of the temperature and their influence on wind regime in a confluence zone of Antarctica. *Meteorology and Atmospheric Physics*, **70**, 133–140.
- WENDLER, G., ISHIKAWA, N. & KODAMA, Y. 1988. The heat-balance of the icy slope of Adélie Land, Eastern Antarctica. *Journal of Applied Meteorology*, **27**, 52–65.
- WISCOMBE, W.J. & WARREN, S.G. 1980. A model for the spectral albedo of snow. I: Pure snow. *Journal of Atmospheric Science*, **37**, 2712–2733.

